



# Study of spatial thermal distribution of gold nanourchins in saline by combined transverse probe beam deflection and beam wavefront sensor: biomedical implications

Mohammad E. Khosroshahi<sup>1,2</sup>

Received: 20 June 2019 / Accepted: 29 October 2019 / Published online: 13 November 2019  
© Springer-Verlag GmbH Germany, part of Springer Nature 2019

## Abstract

Combined probe beam deflection (PBD) and wavefront sensor (WFS) technique are used to investigate the thermal distribution of gold nanourchins (GNU) in physiological saline (PS) using a low-power continuous NIR diode laser. Three different samples were prepared for the experiment: (S1) 0.5 mg/mL GNU only, (S2) 0.5 mL PS and 0.3 mL GNU, and (S3) 0.5 mL PS and 0.1 mL GNU. The laser transmission initially increases linearly as  $S3 > S2 > S1$ , but reaches a plateau and remains constant. The probe beam response in an adjective statistics process exhibited a stochastic behaviour at different positions and constant power in  $x$ - and  $y$ -directions. The beam view profiles showed a non-uniform intensity distribution and the addition of PS dramatically caused a blue shift indicating its cooling effect,  $S1(20)$  warmer  $> S1(10)$  medium  $> S2(20)$  cooler.  $S1(10)$ ,  $S1(20)$ , and  $S2(20)$  correspond to the samples irradiated with the laser power (mW) shown in the bracket. The peak-to-valley (PV) and root-mean-square (RMS) values demonstrated a non-linear intensity distribution during the scanning process. The greater PV values in deeper positions may well due to agglomeration, hence the sedimentation process. The Zernike coefficients with high absolute values represent the aberrations that cause the greatest distortion of the wavefront and found in the order of  $S2(20) > S1(10) > S1(20)$ . This is consistent with PV wavefront slope and spatial period aberration relation. The opto-thermal coefficients were obtained as  $S2 (-7.86 \times 10^{-4}) > S3: 0.5 \text{ mL PS and } 0.1 \text{ ml GNU } (-6.3 \times 10^{-4})$ , respectively.

## 1 Introduction

Recently, there have been growing interests in the opto-thermal properties of nanoparticles in a wide variety of industrial and biomedical applications including photonic devices [1], plasmonic devices [2], surfaced-enhanced spectroscopy [3], biochemical sensing [4], biomedical imaging [5, 6], and photothermal therapy [7–10]. This is mainly because of the unique optical properties of plasmonic nanoparticles (PNP) whose electron density can couple with electromagnetic radiation with wavelengths much larger than the nanoparticle dimension [11]. Upon interaction of the electromagnetic wave with PNP, the conduction band electrons are excited leading to a coherent oscillation which exhibits strong

optical absorption and scattering due to localized surface plasmon resonance (LSPR) [12]. Because of the plasmon oscillation, a dipole is induced which enhances the local electric field at the surface of PNP, and hence, a strong light absorption and scattering occurs at the SPR frequency, which is also temperature-dependent [13]. The absorbance and scattering cross sections describe the intensity of absorbed or scattered light at a given frequency. The heat produced by the PNP is due to the absorption of incident photons and conversion of photon energy into heat energy, and eventually is transferred to the surrounding matrix. It is this process that forms the basis of photothermal application of PNP in biomedical applications [14]. However, depending on the size and the shape of these particles, one can also select appropriate particles for bioimaging where the scattering becomes dominant unlike absorption in the case of heating effect with an exception in the case of photoacoustic where the absorption plays a key role in imaging [15].

In some biomedical applications, the PNP is employed as colloidal particles in liquids (e.g., blood) where factors such as the dispersion quality, agglomeration, and sedimentation are important issues to be considered [16–19]. Another

✉ Mohammad E. Khosroshahi  
m.khosro@miselectronics.com; khosrom@mie.utoronto.ca

<sup>1</sup> Nanobiophotonics and Biomedical Research Laboratory, MIS-Electronics Inc., Richmond Hill, Canada

<sup>2</sup> Department of Mechanical and Industrial Engineering, University of Toronto, Toronto, Canada

example is when the PNP is accumulated or aggregated on the surface of cells resulting in a significant decrease of bubble formation threshold, thus increasing the efficiency of cancer cell killing at lower laser energy [20–22]. Also, in the laser hyperthermia of tumour, it is aimed to minimize the healthy tissue damage surrounding the target. To achieve this objective, an acceptable distribution of PNPs and a precise resolution of temporal and spatial heat transfer problems in practical conditions are needed to be considered [23–25]. Recently, there has been a great advance in synthesis and biomedical applications of new nanostructures with different shapes such as gold nanostars in optical imaging [26] and sensing [27] notably because of enhanced surface-enhanced Raman spectroscopy (SERS) for disease detection and therapy due to enhanced heating effect [28, 29]. GNU has unique optical properties compared to spherical gold nanoparticles of the same core diameter where the spiky uneven surface causes a redshift in the surface plasmon peak and a larger enhancement of the electromagnetic field at the tips of the GNU spikes [30]. Also, GNU with 100 nm diameter as in our case, have an SPR at 680 nm compared to 530 nm of spherical gold nanoparticles, thus make them more suitable to be used with 800 nm diode laser which is frequently employed in biomedical applications due to its higher photon penetration depth within the therapeutic window ( $\approx 700\text{--}1300$ ) at isosbestic point, i.e., where hemoglobin and oxyhemoglobin show the same absorbance [31].

Some well-established techniques that have been used to study the thermal properties and chemical analysis of transparent materials include photothermal deflection spectroscopy (PTDS) [32, 33], photothermal lensing spectroscopy (PTLS) [34, 35], and z-scan [36, 37] using either pulse or continuous lasers. The underlying principle of PTDS is based on the absorption of laser energy by the medium resulting in the local heating and temperature fluctuation at the irradiated region, which causes a change in the refractive index of the medium due to thermal distribution. In our case, the medium also contains nanoparticles, which act as an individual absorbing center and the medium effectively becomes strongly inhomogeneous. There are two possible cases in PTDS: (a) the change in thermal refractive index of medium caused by the pump beam affects its own propagation within the medium, resulting in self-defocusing effect, because the derivatives of the refractive index with temperature is usually negative, so that the temperature gradient produces a negative lens, (b) it affects the propagation of another beam, i.e., the probe beam in the vicinity of the pump beam called probe beam deflection PBD [38]. The PTDS signal caused by the thermal lens volume is dependent on the spatially dependent refractive index change produced by temperature change. While, in PTLS configuration, the probe beam is collinear with the pump beam, in PBD, the probe beam can be used in either parallel or transverse geometry [38]. In the

latter case, the temperature gradient created by the pump beam is symmetrical not with respect to the probe beam axis, but perpendicular to it. Thus, by probing the gradient of the varying index of refraction due to temperature or concentration variation with the probe beam, one can relate its deflection to the optical absorption of the sample. A CMOS-based wavefront sensor with a wide range of spectral sensitivity can also be used to provide accurate measurements of the wavefront shape and the intensity distribution of optical beams, and has been widely applied in optics [39, 40] characterization of non-linear materials [41], imaging [42, 43], and ophthalmology [44] to reconstruct the optical path length difference between rays in the focal plane using the derivatives of the wavefront which is Zernike polynomials. In this work, the opto-thermal properties of GNU in PS irradiated by fibre-delivered continuous near-IR laser (808 nm) are investigated by combined transverse-mode deflection and WFS technique. The work provides some information regarding the behaviour and thermal intensity distribution of nanoparticles in PS, which can have some biomedical implications such as tumour laser hyperthermia where the distribution of nanoparticles and hence their thermal effects within the cells directly affect the efficacy of tumour destruction. Besides, the dispersion or agglomeration of nanoparticles, which influences the amplitude of thermal intensity, must be considered. The combined approach is believed to be the unique feature of this research.

## 2 Experimental

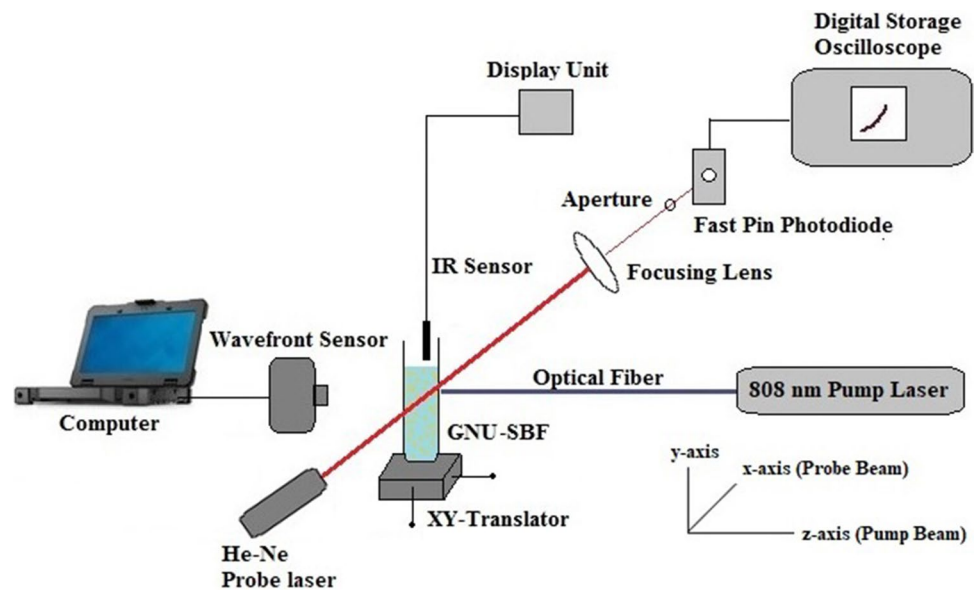
### 2.1 Materials and methods

20 mL GNU with 100 nm diameter,  $3.84 \times 10^9$  NP/mL, and weight concentration of  $3.89 \times 10^{-2}$  mg/mL dispersed in 0.1 mM phosphate-buffered saline were purchased from Cytodiagnosics (GU-100-20-Canada). The absorbance was measured by UV–Vis spectrometer (Jenway-Cole-Parmer-Canada) with 198–1000 nm spectral range. Physiological saline was purchased from a local drug store. Three different samples were prepared for the experiment: (S1) 0.5 mg/mL GNU only, (S2) 0.5 mL PS and 0.3 mL GNU, and (S3) 0.5 mL PS and 0.1 mL GNU. S1 (10), S1 (20), and S2 (20) correspond to the samples irradiated with the laser power (mW) shown in the bracket.

### 2.2 Experiment

Prior to the PTDS experiment shown in Fig. 1, the absorbance of GNU was first recorded separately by UV–Vis spectrometer ((JENWAY-7205) between 200 and 900 nm, and the laser power transmission in PS at different concentrations of GNU was measured by a dual-channel benchtop

Fig. 1 Experimental setup



pyroelectric energy/power meter (ES220C, PM 320E-Thorlabs). The experimental setup is illustrated in Fig. 1 where a quartz cuvette (Cole-Parmer-Canada) with a width of 1 cm containing the solution was mounted on an  $x$ - $y$  translation stage (XYT1-Thor Labs-Canada) for scanning purpose and a four-channel fibre-coupled laser (MCLs1, Thor Labs-Canada) with a stable, low noise and 25 mW output operating at 808 nm was delivered through a 400  $\mu\text{m}$  core diameter fused silica optical cable with a and 0.39 numerical aperture (Thor Labs-Canada).

The pump-probe beam configuration was kept constant at an orthogonal angle and the sample as moved for scanning. Thus, each position as a new reading produced a thermal distribution corresponding to that point. A non-contact IR sensor (Omega-OS36-50F) was used to measure the temperature before and during the experiment. A 1 mW He-Ne laser (R-36602-Newport) was used as probe beam in transverse configuration to monitor the heated region by the pump laser, which was then focused by a 100 mm CaF convex lens on to a fast pin Si photodiode (BPX-65-RS-UK) with responsivity of 300–1100 nm via an aperture to increase the sensitivity of output signal displaced on a 300 MHz digital storage oscilloscope (BK-Precision-UK). The signal is detected as the relative probe beam transmission change through a small aperture located in the far field. A CMOS-based Shack-Hartmann wavefront sensor (WFS150-50C-ThorLabs-Canada) with 300–1100 nm spectral sensitivity is utilized to study the wavefront shape and the intensity distribution of optical beams. During the operation, the WFS was placed behind the cuvette with its entrance aperture facing directly the incident pump beam, so that the microlens array of the sensor creates a matrix of focal spots on a CMOS camera. Flat wavefront looks at

the camera as an absolute correct grid of light spots, but when the analyzed wavefront is distorted, the light spots are located irregularly. Displacement of each spot from the reference position is proportional to the derivative of the wavefront in each of the microlenses. Therefore, the wavefront is reconstructed from the values of the displacement of light spots and the aberrations are calculated [38]. To reduce the unwanted reflections back into the source, the WFS can be slightly tilted. An off-center beam can be measured provided that the full beam is contained within the active sensor area, which can be checked if the power density distribution displayed in the beam view panel. It is noteworthy that WFS sensitivity is strongly wavelength-dependent and decreases considerably particularly in the range of (400–900 nm), thus higher power beams with wavelengths overlapping these lower sensitivity ranges can be measured directly. The WFS application software, which controls the image acquisition, analyzes the centroid locations of the focal spots and provides wavefront measurements, which are then saved and analyzed by a computer.

### 3 Results and discussion

The UV-Vis absorbance spectrum in Fig. 2a shows the SPR for S1 at about 680 nm which gradually reduces to 800 nm with a noticeable intensity of  $\approx 60\%$ . Nevertheless, it seems to be sufficient and more efficient than spherical gold nanoparticles for heat generation at NIR wavelength due to the proximity of SPR [30]. Prior to the transmission experiment, the temperature of the samples was measured before and after the experiment. The temperature for direct fibre output-IR sensor at 20 mW at room temperature

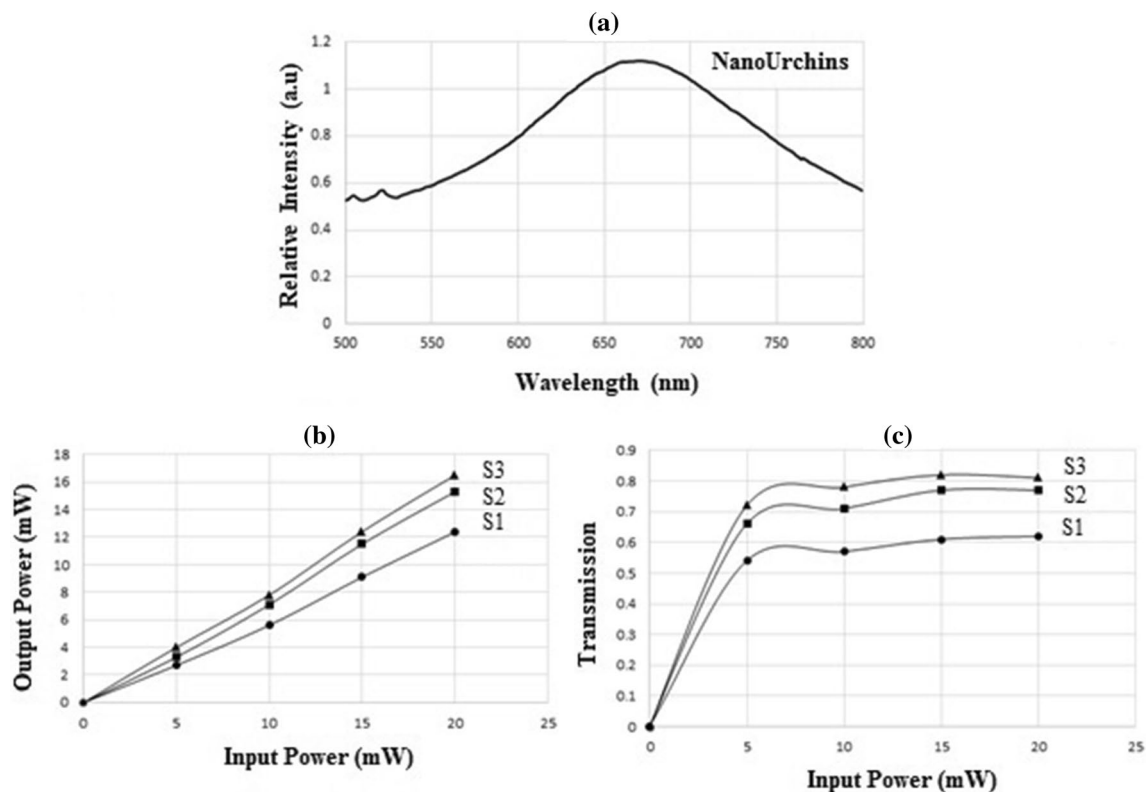


**Fig. 2** a UV-Vis spectrum of gold nanourchins b variation of laser output power with input for S1 (GNU only), S2 (0.3 mg/ml) and S3 (0.1 mg/ml) and c variation of power transmission with laser input power

(15.5–16 °C) without a sample was measured 23 °C, and that for S1 and S2 were 18–18.5 °C and 16–16.5 °C, respectively, i.e.,  $\approx 2$  °C higher for pure GNS and  $\approx 1$  °C higher in the case of higher concentration of 0.3 mg mL<sup>-1</sup> than room temperature. The laser power entering and exiting the sample was measured by the power meter to determine the power transmission. The variation of output with input power was studied for all the samples. The volume fraction,  $V_f$ , of the GNU is given by:

$$V_f = \frac{V_p}{V_p + V_{ps}} \times 100, \quad (1)$$

where  $V_p$  and  $V_{ps}$  are the volumes of GNU and PS, respectively. Using Eq. (1) gives the values of  $37.5 \times 10^{-2}\%$  and  $16.7 \times 10^{-2}\%$  for S2 and for S3, respectively, which shows the effect of higher GNU concentration. It is seen from Fig. 2b that the variation is linear in all cases and that S3 exhibits the highest output due to a lower weight concentration of  $6.48 \times 10^{-3}$  mg mL<sup>-1</sup>, i.e., more diluted compared to S1 and S2. Figure 2c indicates that the transmission increases linearly up to 5 W due to higher output energy of ballistic photons detected which then reaches a plateau and remains almost constant. The higher transmission for

S2 and S3 is because of lower GNU concentration due to dilution, thus higher ballistic photons travel in medium, i.e., less photons random walk. Therefore, according to Rayleigh scattering, the intensity of scattered light is proportional to the square of the volume of particles and the number of scattering centers, which should be proportional to the concentration of scattering particles in any given sample. However, when the size of the scattering centers approaches to or become greater than the light wavelength, Mie scattering occurs where the intensity of scattered light is symmetric about the particle. The maximum transmission of 80%, 70% and 55% was achieved for S3, S2, and S1, respectively. Using the Beer–Lambert law, the attenuation coefficients of about 0.35, 0.4, and 0.6 cm<sup>-1</sup> are obtained for S3, S2, and S1, respectively, indicating that the optical penetration depth decreases with increasing the GNU concentration. The direct biomedical implication of this would be the generation of a variable amount of heat as a function of concentration, which is also determined by the target depth.

Figure 3 indicates the typical photodiode signal response for S1 to the beam passing through 1 mm aperture where the cuvette continually moved in a certain distance along  $x$ -direction, while the pump and probe beams were orthogonal and kept constant. Therefore, the scanned distances

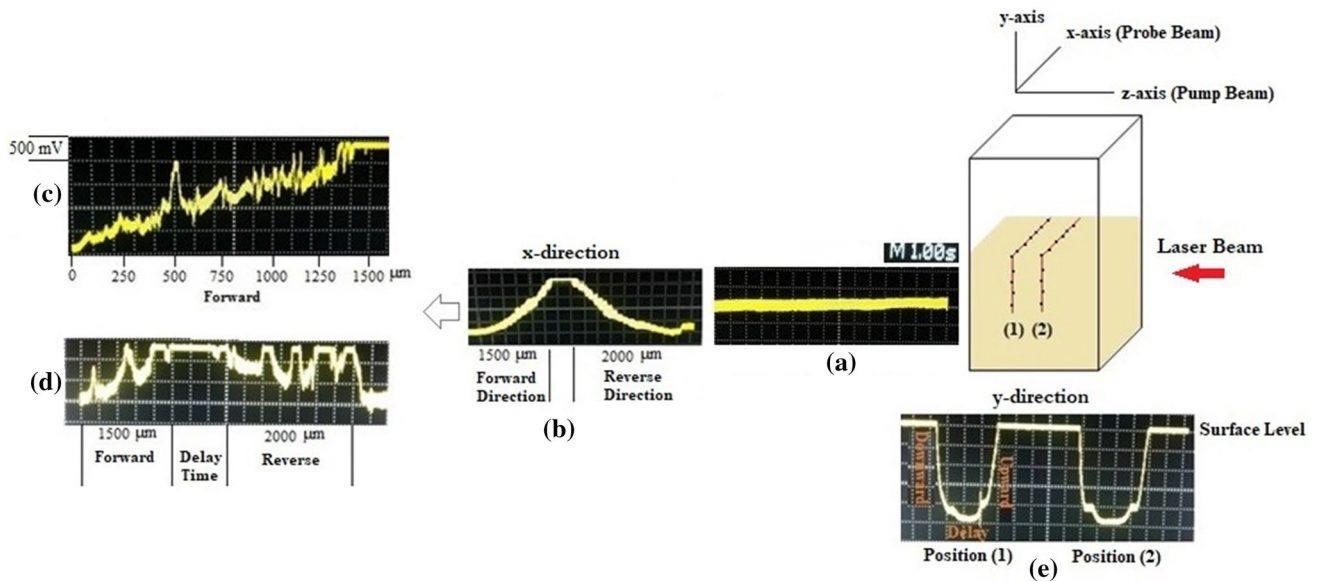


**Fig. 3** Schematic representation of laser scanning of cuvette at different positions **a** base line signal **b** an example of continuous scanning response in forward and reverse directions **c** the photodiode response at position (1) in forward direction showing complete random varia-

tions **d** same as **c** at position (2) and **e** U-shape photodiode response in *y*-direction for S2 at positions (1) and (2) in forward and reverse directions

represent a new position with different GNU population distribution with respect to the initial point. Figure 3a shows the baseline and the photodiode response within a distance of 1500  $\mu\text{m}$  in forward and reverse *x*-directions corresponding to the position (1) is shown in Fig. 3b. The demographic stochasticity of the photodiode response in Fig. 3c demonstrates, first, the randomness of the results with a steadily increasing trend of the curve with a sharp peak at  $\approx 500 \mu\text{m}$  likely due to a non-uniform distribution of GNU. One possible reason for such a behaviour of the curve is that the scanning speed is higher than the thermal relaxation of the medium to allow it to settle down to the baseline before the next recording. Second, every spike represents a new location with a density of GNP at that particular instant of time and position during the interaction. The amplitude of the spikes implies the density distribution and hence the corresponding response. Similarly, Fig. 3d represents the corresponding variations in position (2) with two major peaks at about 300 and 800  $\mu\text{m}$ . However, as it is observed, the irreversible variations in reverse direction compared to the forward direction indicate the statistically random nature of GNU distribution. Figure 3e shows when the cuvette was moved up and down in the *y*-direction in two different positions and producing a U-shape result for forward and reverse directions within  $\approx 1500 \mu\text{m}$  distance. It is noteworthy that the data in both *x*- and *y*-directions at positions (1) and (2) are recorded in an adjective statistics process that is a randomly determined sequence of observation where each data set corresponding to a given point at that position

is considered as a sample of one element (i.e., the cuvette) from a probability distribution.

Figure 4a shows the corresponding signal changes with scanned distance in *x*-direction seen in Fig. 3c at position (1) where the deflection increases steadily with a sharp peak at  $\approx 500 \mu\text{m}$ . Similarly, Fig. 4b represents the corresponding variations in Fig. 3d at position (2) where again the signal increases up to  $\approx 300 \mu\text{m}$ , which begins to deviate from linearity up to  $\approx 600 \mu\text{m}$ ; thereafter, it remains constant or saturated by increasing the distance. The random distribution of GNU is illustrated schematically in Fig. 4c where it is assumed after introducing into the center of the cuvette, and they gradually tend to distribute as gaussian mainly under the influence of Brownian motion. The non-uniform distribution of GNU within the solution and possible interference of enhanced laser thermal waves is schematically shown in Fig. 4d. The random nature of such distribution and spatial fluctuation within the solution causes some degree of thermal wave intensity modulation. Thus, the net effect is a stochastic modulated spatial intensity distribution with strong and weak points within the medium. It is known from Stokes hydrodynamic forces that each moving particle generates a velocity field in the surrounding medium. Given the particle position at time  $t$ , the positional shift  $\vec{r}_i(t + \Delta t) - \vec{r}_i(t)$  of each particle is determined by  $\vec{v}_i \cdot \Delta t + \vec{\xi}_i$  where  $\vec{r}_i$  is NP  $i$  in position  $r$ ,  $\vec{v}_i$  is the velocity of NP  $i$ , and  $\vec{\xi}_i$  is the shift due to Brownian motion determined from a Gaussian distribution of randomly distributed NPs within solution. The diffusion time is given by [45]:

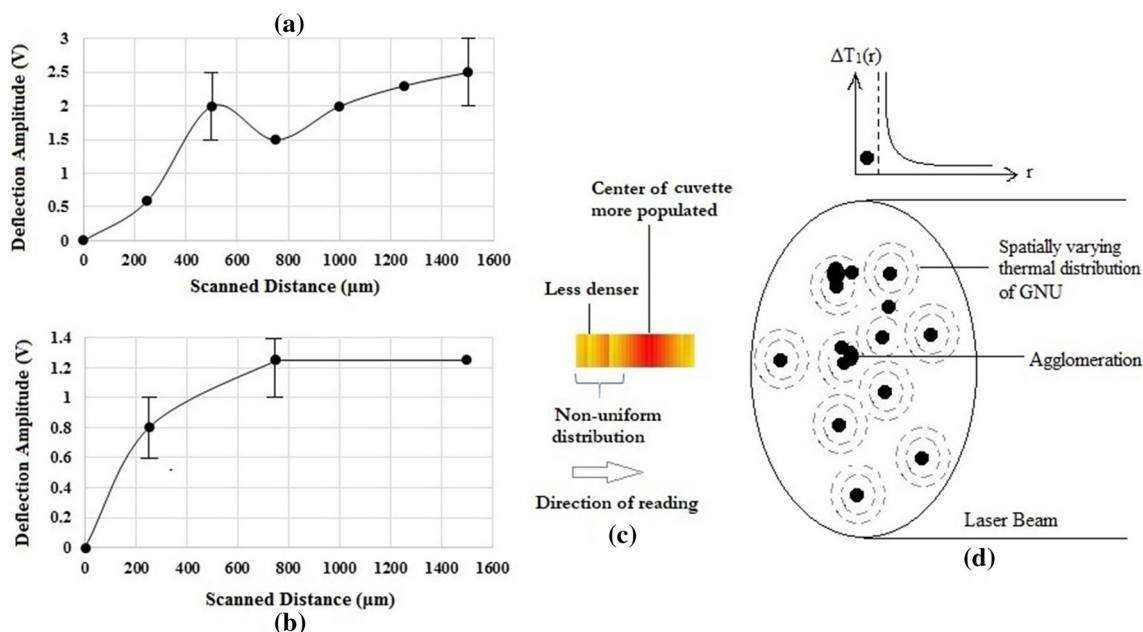


**Fig. 4** Variation of photodiode voltage amplitudes with scanned distance **a** at position (1) and **b** at position (2) **c** schematic representation of gaussian radial distribution of GNU where the number density

decreases outward and **d** schematic representation of non-uniform distribution with possible agglomeration of GNU

$$t_d = \frac{18\pi\eta R_p^3}{k_B T}, \tag{2}$$

where  $\eta = 1 \text{ m}^2 \text{ s}^{-1}$  is PS viscosity,  $R_p = 50 \text{ nm}$  is the GNU radius,  $k_B = 1.38 \times 10^{-23} \text{ J K}^{-1}$  is Boltzmann constant, and  $T \approx 16 \text{ }^\circ\text{C}$  is the room temperature at the time of the experiment. Substituting the values in Eq. (2) gives  $t_d \approx 1.77 \text{ s}$ . The reading is taken from left to right starting from closer to the cuvette’s wall towards the center where it is believed that the signals become stronger due to the denser medium in the vicinity of the center as well as the possible change in the size of nanoparticles. The same argument applies to the y-axis except that here sedimentation can also affect the results.

The agglomeration or clustering can be formed by (a) particle–fluid interactions, which play a role in the motion of nanoparticles and (b) particle–particle interactions, which control whether colliding particles will adhere (attraction) or bounce off (repulsion). This is explained by DLVO (Derjaguin, Landau, Verwey, and Overbeck) theory, which defines inter-particle forces as the sum of van der Waals and double-layer electrostatic contributions [46, 47]. The variation of nanoparticles with time due to agglomeration is [48]:

$$-\frac{dN_{np}}{dt} = kN^n, \tag{3}$$

where

$$k = Ae^{-E_a/RT}, \tag{4}$$

is the agglomeration rate of the coefficient defined by Arrhenius equation,  $A$  is a pre-exponential factor,  $E_a$  is the activation energy,  $R$  is the molar gas constant, and  $T$  is the temperature,  $N$  is the number of nanoparticles and  $n$  is the reaction order. The agglomerate size increases with increasing the temperature due to increasing the van der Waals cohesive force, which is caused by fluctuating electric dipoles and decay asymptotically as  $r^{-7}$ , where  $r$  is the distance between the particle centers. On short distances, the force diverges like,  $d^{-2} = (r - 2R_p)^{-2}$ , where  $R_p$  is the radius of NP and  $d$  is the distance between the surfaces. The equilibrium aggregate number density distributions may be obtained by considering the combined consequences of agglomeration break-up and the integrating it over time for a steady-state time solution. The cluster size,  $s(t)$ , is determined by the average number of NPs in agglomerates [49]:

$$s(t) = \frac{N_0}{G(t)}, \tag{5}$$

where  $G(t)$  is the total number of agglomerates per unit volume in the ensemble at time  $t$  and  $N_0$  is the total number of NPs per unit volume in the ensemble. For nanoparticles in a dispersed state, the van der Waals force is neglected. Therefore, in contrast to the thermal effect, the optical scattering which, is independent of type of material is caused by the inhomogeneity in the refractive index of the medium, the

spatial distribution of the scattering, the size, and the shape of the inhomogeneity (i.e., NPs) relative to the source wavelength. In this case, the size factor  $x = 2\pi R_p/\lambda \approx 0.4 < 1$ , and thus, Rayleigh scattering can apply provided anisotropy factor  $g = 0$ . However, when the particle size increases due to for an example, clustering then the intensity distribution increases,  $g \rightarrow 1$ , and the scattering phase function for small angles becomes much higher than for all other angles.

The beam view panel provides an overview of the intensity distribution within the active camera sensor area. Different colours in the spectrum represent the intensity distribution in the beam caused by the interaction region detected by WFS. Black and purple show the lowest beam

distortion due to low intensity hence lower thermal distribution within the solution, green shows the medium distortion, and the red and white represent the highest distorted parts. Each point of the displayed intensity array is derived from the calculated mean intensity of the corresponding spot. As it is seen, the intensity and hence the temperature distribution during the laser interaction in solution vary quite non-uniformly. This is because in a random colloidal system of PNPs, there are the so-called ‘hot’ spots where the electric field and heating intensity are considerably increased and the spiky feature of GNU will enhance this effect. Therefore, such a system can be used to strongly increase the heating intensity at certain points [50].

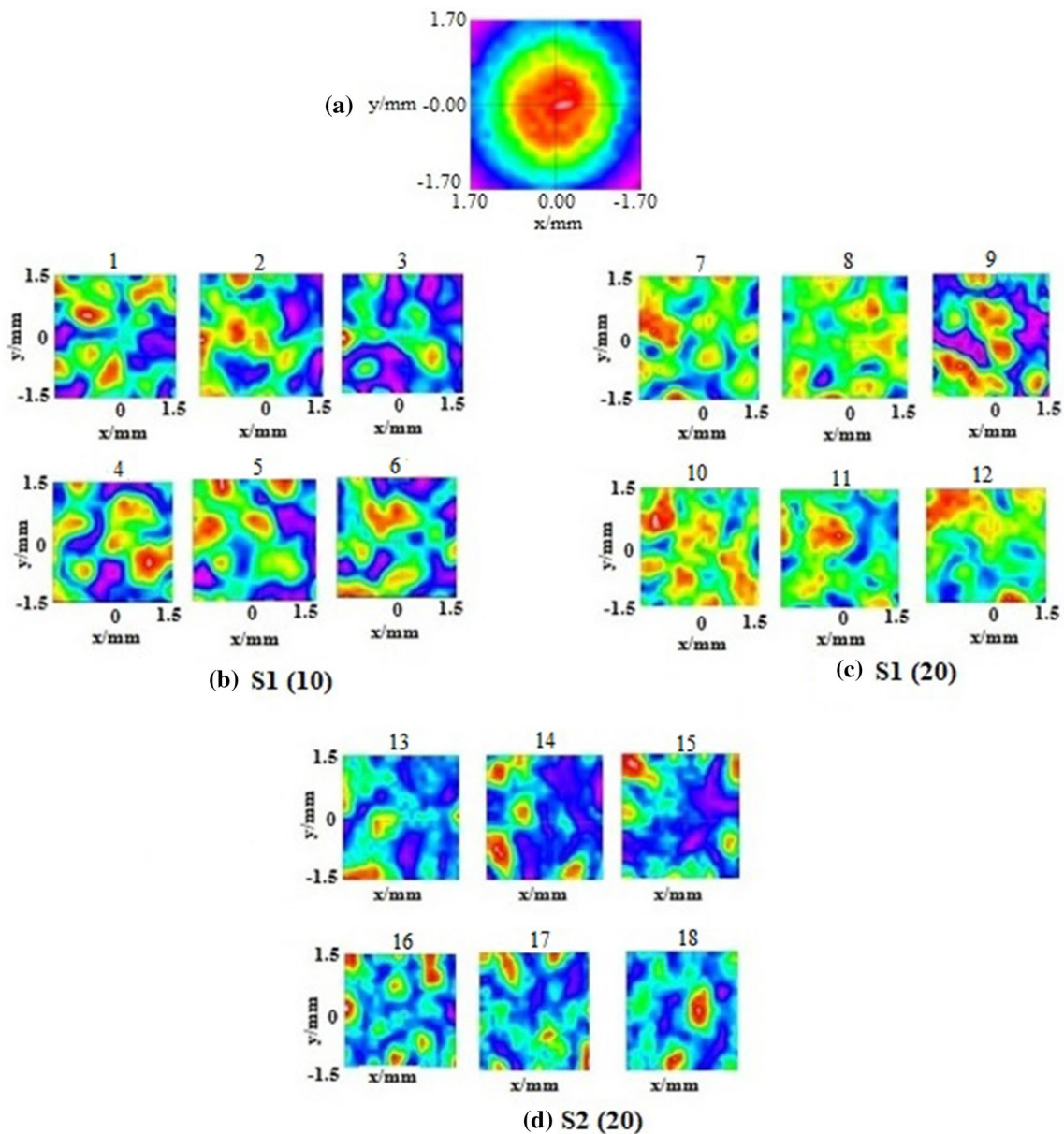


**Fig. 5** Beam view profiles for **a** direct pump beam **b** S1(10) **c** S1 (20) **d** S2(20). Note that longer wavelengths of red and green demonstrate the warmer regions and the shorter wavelengths the cooler regions

Figure 5a represents the beam view of a laser from optical fibre output without cuvette. Figure 5b illustrates the beam view profiles for S1 (10) at different scanned distances relative to the position of the first reading where each interval of reading is about 250  $\mu\text{m}$ . As it is observed, the profiles consist of a combination of different colours indicating the randomly distributed thermal regions, such that Fig. 5(1), (2) have warmer patches than Fig. 5(3) with a bluer colour which is cooler. However, as discussed above, when the cuvette moved towards the center, an intense red patch was observed at  $\approx 1000 \mu\text{m}$ , Fig. 5b (4), due to a more localized GNU population which gives rise to a higher temperature. Further away between 1500 and 2000  $\mu\text{m}$  corresponding to Fig. 5b (5) and (6), the red colour diminishes and the distribution appears to be slightly less intense again.

The experiment was repeated for S1 (20), as shown in Fig. 5c, where the colours mainly show high and intense intensity distribution within the solution. Figure 5c (7) as the first reading indicates a red region with mostly dominated green colour followed by a medium-type background dominated with green and yellow colours and less cool (blue colour) regions at 500  $\mu\text{m}$  in Fig. 5c (8). However, at 750  $\mu\text{m}$  Fig. 5c (9), it becomes dominantly purple indicating a very low degree of temperature distribution, hence the very little effect on the beam profile. Beyond this point closer to the center, the profiles display dominantly warmer colours as seen in Figs. 5c (10–12). The last experiment was performed with S2 (20), as illustrated in Fig. 5d. Clearly, as expected, the presence of PS greatly has reduced the temperature of the solution during the laser interaction. It is seen in all Fig. 5d (13–19) that purple is the most dominant colour throughout the entire scanned distance. Again, while there is an irregular and random distribution, Fig. 5d (15) and (16) produced the least intense images at 250 and 500  $\mu\text{m}$  positions, but it gradually becomes intense at further distances. The PV indicates the wavefront distortion due to the fluctuation of aberration caused by the thermal effects in the colloidal solution. PV is estimated from the highest and lowest points on the

wavefront surface relative to the reference surface. The root-mean-square (RMS) error in the diffracted spot from different apertures of the sensor is an area-weighted statistics, which is calculated as the standard deviations of the height of the test surface relative to the reference at all the data points in the wavefront surface. It is possible to have errors in the measurement of the diffracted spot locations that are larger due to various factors. The values of PV and RMS given in Fig. 5 are plotted in Fig. 6a, b, respectively. They show that the aberrations are initially higher, but decrease at distances further away with respect to the initial position for S1 (10) and S1 (20) until a turning point, i.e., minimum is reached at  $\approx 1000 \mu\text{m}$ , beyond which the curve changes non-linearly and increases again. It is noteworthy that S1 (10) > S2 (20) unlike one might be expected otherwise at higher laser power. This can be explained by the fact that the PV wavefront slope is [51]:

$$\frac{\partial\phi(x)}{\partial x} \approx 2A \sin \frac{2\pi x}{A_{\text{sp}}}, \quad (6)$$

where  $2A$  is the wavefront PV amplitude, and  $(A_{\text{sp}})$  is the spatial period of aberration. Thus, in the case of S1 (20), where the wavefront slope is smaller than S1 (10), it  $(A_{\text{sp}})$  is larger and PV amplitude is lower. Also,  $\frac{\partial\phi(x)}{\partial x} = \frac{r_b}{R_c}$  where  $r_b$  is the spatial radius of the beam and  $R_c$  is the radius of incident wavefront curvature. Assuming that  $r_b$  remains constant, since the slope of Fig. 2c gives an absorption coefficient of  $\alpha \approx 0.51 \text{ cm}^{-1}$ , which gives a penetration depth of almost twice the optical path length or the cuvette length, then  $R_c$  is expected to increase by increasing power, and hence, the slope is reduced, which justifies the observation.

The wavefront panel displays the wavefront as a 3D image. The wavefront data array is received from the spot shifts which are directly proportional to the local derivatives of the wavefront. A 2D integration process, starting at the center spot, leads to the wavefront data. In the case of a

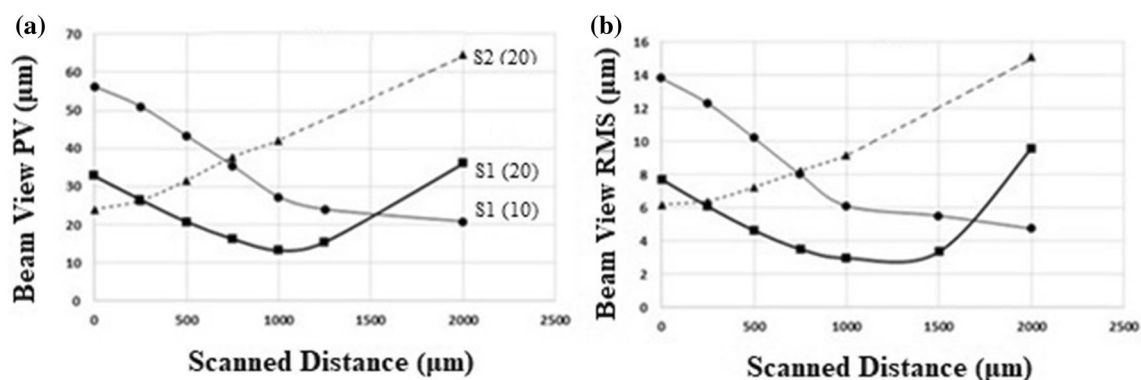


**Fig. 6** Variation of **a** beam view PV and **b** beam view RMS with scanned distance in the order of S2(20) > S1(10) > S1(20) consistent with PV wavefront slope and spatial period aberration relation



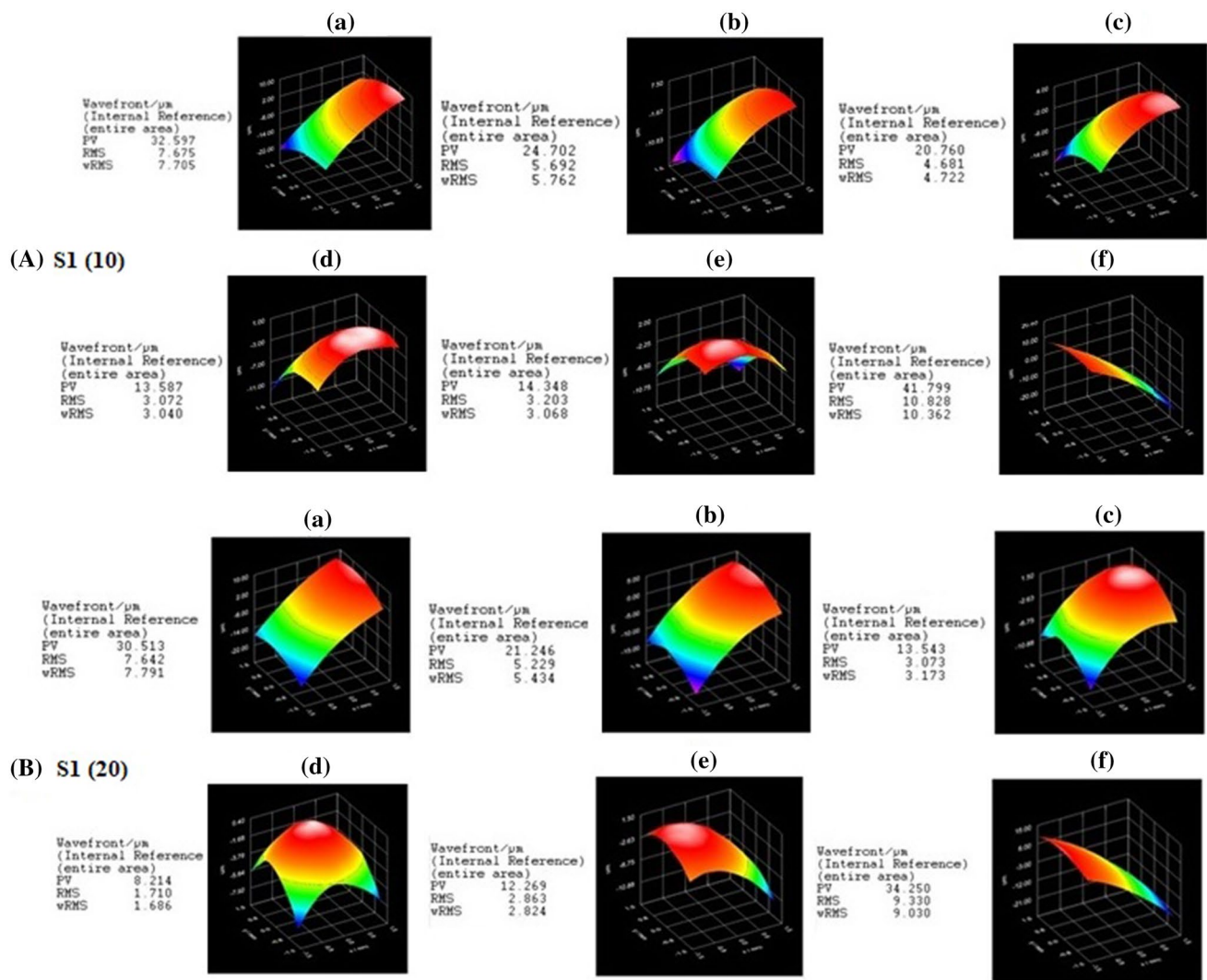


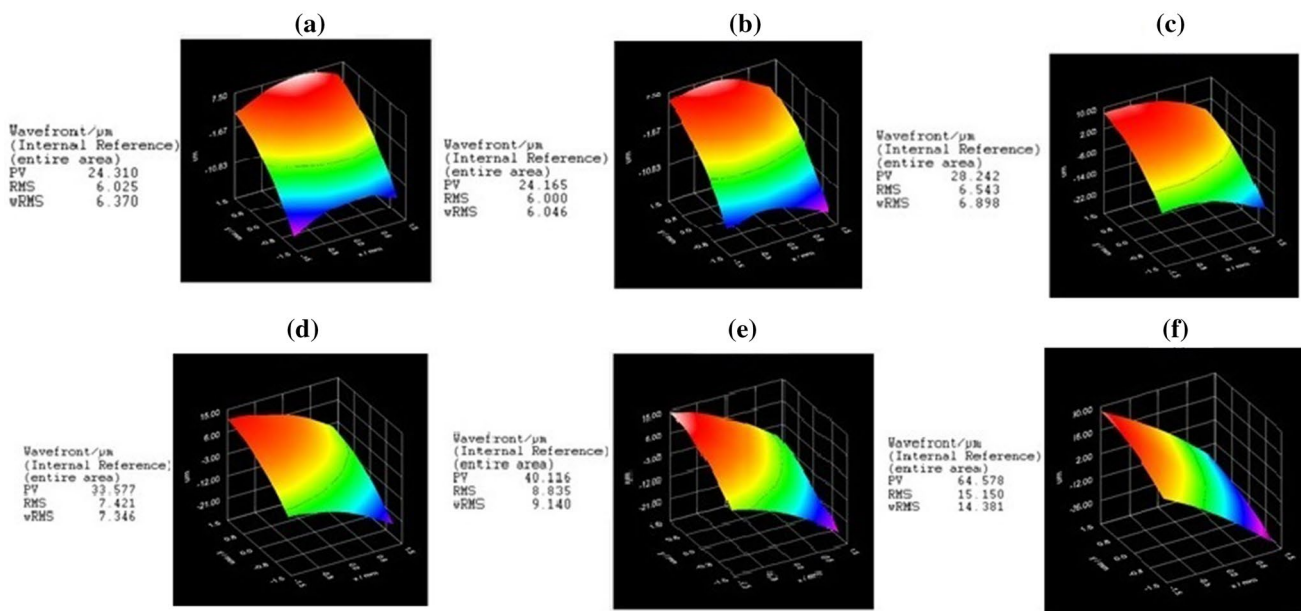
**Fig. 7** Wavefront profiles for (A) S1 (10) and (B) S1 (20) where initially, the PV values decrease with scanned distance but then increase indicating the non-linear behaviour

distorted wavefront incident on the sensor, the focal point positions shift along the  $x$ - and  $y$ -directions, away from the optical axis  $z$  of the microlens. The corresponding observed wavefronts' deformation for S1 (10) and S1 (20) is given in Fig. 7A, B, respectively. As seen, the observed wavefront is distorted by aberration caused by opto-thermal effects, and hence, the light spots are located irregularly. Since, each of the apertures on the array acts like an optical lever, displacing the diffracted spot proportional to the average phase tilt over the aperture, and therefore, the displacement of each spot from the reference position is proportional to the derivative of the wavefront in each of the microlenses. The wavefront is then reconstructed from the values of the displacement of light spots.

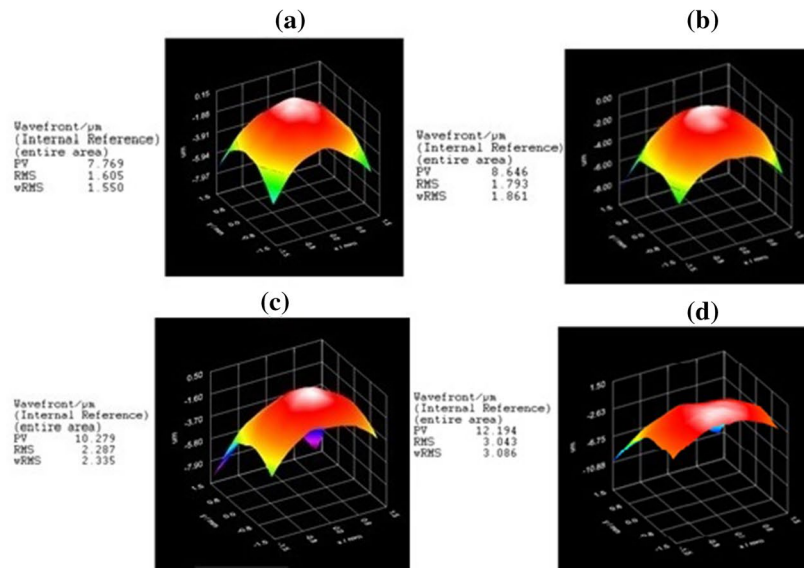
Similarly, the wavefronts for S2 (20) are illustrated in Fig. 8A, where the least distortion occurs at the initial

position, Fig. (a), and it increases up to  $2000 \mu\text{m}$  as seen in Fig. (f). The results corresponding to the  $y$ -axis are shown in Fig. 8B where the fewer fluctuations occur near the surface, Fig. 8B (a) compared to the deeper positions Fig. 8B (d) as explained above.

The corresponding values of PV and RMS related to Figs. 7 and 8 are given in Fig. 9, which demonstrates a similar non-linear behaviour as in Fig. 6. Figure 9 shows that the PV (a) and RMS (b) fluctuation gradually decreases for both S1 (10) and S1 (20) up to  $\approx 750 \mu\text{m}$  beyond which it begins to increase again. In contrast, the distortion in S2 (20) began earlier and increased linearly without a turning point in the present experiment condition. Interestingly, in the case of S2 (20), Fig. 9c, the distortions closer to the surface in the  $y$ -axis are smaller than those at the deeper positions. This can be because of higher GNU number density at deeper



(A) S2 (20)



(B) S2 (20)

**Fig. 8** Wavefront profiles for (A) S2 (20) in x-direction and (B) S2 (20) in y-direction where initially, the PV values decrease with scanned distance but then increase indicating the non-linear behaviour

locations due to sedimentation. Self-assembly of NPS under influence of electromagnetic field with the frequencies in the optical range has been studied [52], and when NPs are irradiated by the laser radiation, dipole moment is induced which enhances the formation of structural geometry, the nanoparticles suspended in a base fluid experience interparticle collision, and attachment of the colliding particles to form aggregates [53]. Therefore, the sedimentation process which is influenced by the gravity field gradually occurs

and it is expected to have a stronger probe beam deflection in y-axis [49]. In the case of Brownian dynamics (i.e., no pump laser), trajectories of an ensemble of NPs in the base medium are described by well-known Langevin equation where the interaction between NPs with the environment with fluctuating density results in a random change of trajectory movement. It has also been shown that photoacoustic signals, which is due to the absorption of radiation energy by PNP and hence the generation of thermoelastic waves,

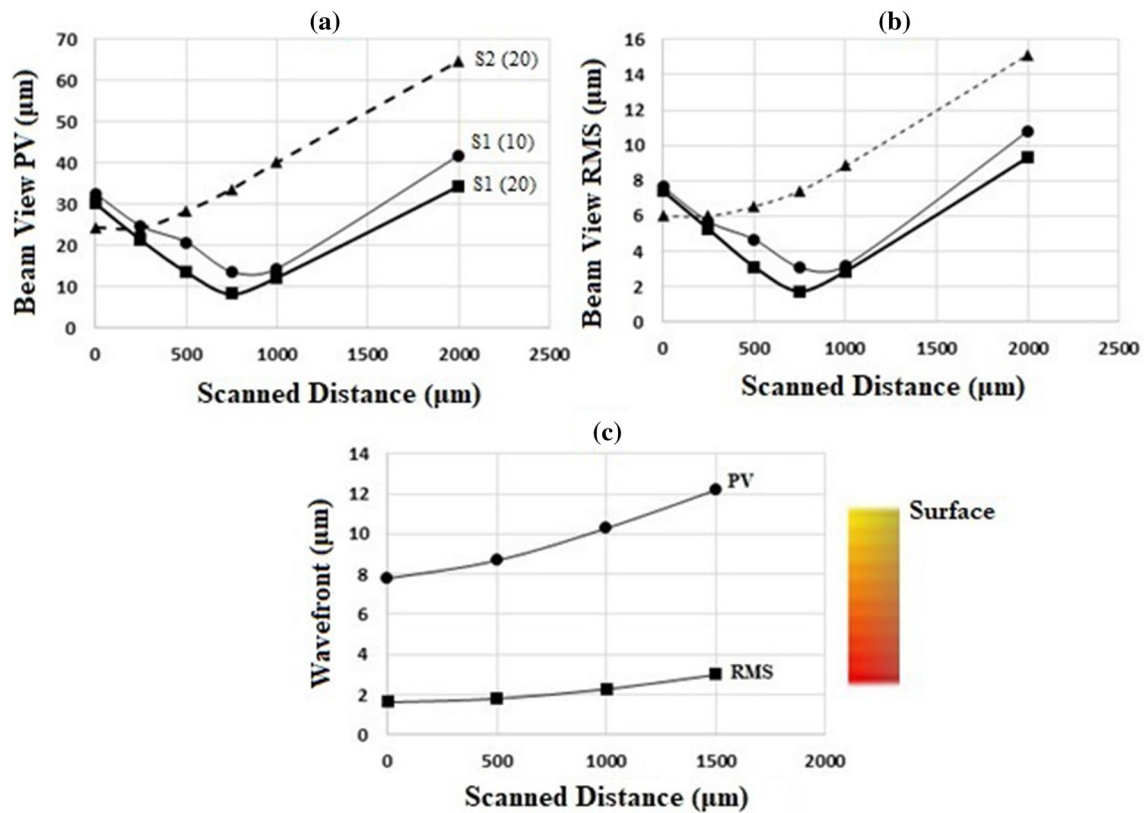


Fig. 9 Variation of wavefront a PV b RMS with scanned distance in the order of S2(20) > S1(10) > S1(20) and c in y-direction

increase by agglomeration of nanoparticles, i.e., the agglomeration ensemble can act as photonic amplifier [54]. The settling velocity of GNU during the sedimentation process under the influence of gravitational force can be determined by [55]:

$$V_s = \frac{\phi_p(\rho_f - \rho_p)g}{18\eta}, \tag{7}$$

where  $\phi_p$  is the GNU diameter,  $\rho_f = 1000 \text{ kg m}^{-3}$  is the PS density, and  $\rho_p = 19,320 \text{ kg m}^{-3}$  is the nanoparticle density, so a value of  $V_s \approx 1 \text{ mm s}^{-1}$  is obtained. Thus, stronger PRB deflection is expected at deeper positions as it is confirmed by the wavefront images shown in Fig. 8B where the values of PV increase with depth as seen in Fig. 9c.

The coefficients of the Zernike modes which are determined by a least-square fit to the measured wavefront are displayed either in microns or waves. The Zernike coefficients represent positive or negative amplitude, and indicate that the measured wavefront contains particular Zernike modes. The resulting coefficients are displayed as a bar graph chart on the Zernike coefficient modes.

By default, the highest Zernike order is set to  $n = 4$  which implies a total number of 15 Zernike modes. The higher the order, the more Zernike modes are used to reconstruct the measured wavefront shape. The change of Zernike coefficients with modes for S1(20), S1(10), and S2(20) are shown in Fig. 10. The coefficients with high absolute values represent the aberrations that cause the greatest distortion of the wavefront, which in this case, the values of distortion decreased in the order shown for the above samples, respectively. The range of values of higher Zernike modes also reduces systematically, which implies that the amount of aberration coefficients is less for the higher order modes than for the lower order modes. In this case, S1(10) and S2(20) show the highest and lowest coefficients, respectively.

### 3.1 Heat generation and transfer

The heat generation involves the absorption of incident photons and consequent conversion into heat energy which then is transferred to the surrounding medium. The interaction of an electromagnetic field:

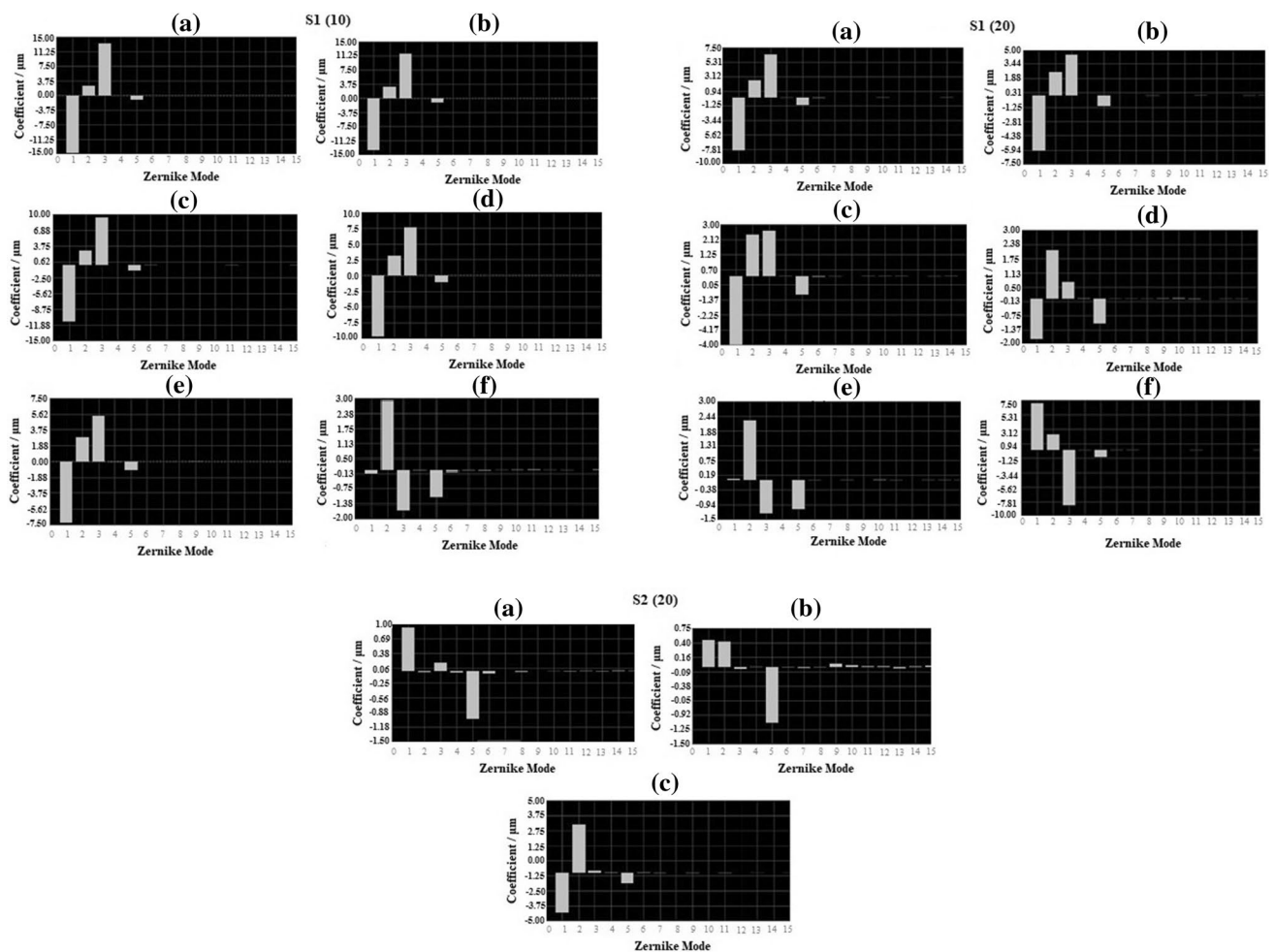


Fig. 10 Variation of Zernike coefficients with modes for S1 (10) with highest, S1(20) intermedium and S2 (20) lowest aberration

$$E(r, t) = [E_0(t)e^{i(kz-\omega t)}], \tag{8}$$

of a laser with PNP, which strongly depends on number of factors such as size, shape, composition of nanoparticles, and the base medium, causes the dielectric polarization of surface charges as a result of which charges oscillate like simple dipole moment nanoparticles where  $\omega$  is the angular frequency of light travelling in the  $z$ -direction and  $k=2\pi/\lambda$  is the wavenumber, where  $\lambda$  is the laser wavelength. The oscillating dipole radiates electromagnetic waves with large enhancement of the local electric field at the nanoparticle surface and polarization proportional to the incident field. This electric field leads to strong absorption and scattering at the SPR frequency by the particle which consequently damps the oscillations, causing the displacement to become out of phase with the varying field and requiring an input of energy to sustain the oscillation. The SPR absorption in PNP is followed by energy relaxation through nonradioactive decay channels. This results in an increase in kinetic energy,

leading to overheating of the local environment around the light-absorbing species. From the slope of Fig. 2c, the absorption coefficient,  $\alpha \approx 0.51 \text{ cm}^{-1}$ , can be estimated, which gives a penetration depth of almost twice the optical path length or the cuvette width,  $L = 1 \text{ cm}$ . Therefore, the beam diameter change can be neglected, i.e., no broadening occurs and the medium is assumed to be thin. As a result, the interaction length,  $d_i$  is supposed to be the same as the beam diameter. The sensitivity of the can be determined by the probe and pump beams rather than the  $L$  where  $\theta=90^\circ$  is the beam crossing angle [56]. This gives  $d_i \approx 360 \mu\text{m}$  which is very close to the fibre diameter.

The complex refractive index,  $\tilde{n}(\omega)$ , is related to its complex dielectric permittivity  $\epsilon_p = \epsilon_r + i\epsilon_i$  through  $\epsilon_p = \tilde{n}^2 = (n_r + ik_e)^2$  where  $n_r = k\lambda/2\pi$  is the real part of the refractive index. The real part  $\epsilon_r = (n_p^2 - k_e^2)$  where  $n_p$  is the real refractive index of NP,  $k_e(\lambda) = \lambda\alpha_p/4\pi$  is the extinction coefficient, and  $\alpha_p$  is NP absorption coefficient at a given wavelength. The imaginary part,  $i\epsilon_i = 2n_pk_e$ ,

which quantifies the relative phase shift of the induced polarization with respect to the external field, determines includes losses ohmic heat loss. The SPR spectral peak position is maximum when  $\epsilon_p + 2\epsilon_s = 0$  where  $\epsilon_p$  and  $\epsilon_s$  are permittivities of GNU and PS, respectively. Taking the values of  $n_p \approx 0.28$  and  $k_e \approx 2.78$  for PNP at 808 nm [57] yields  $\epsilon_r \approx -7.6$  and  $\epsilon_i \approx 1.56$ , and thus,  $\epsilon_p \approx -6$  and  $\epsilon_s = \epsilon_p/2 = -3$ . According to Mie theory, absorption cross section,  $\sigma_\alpha$  and absorption efficiency,  $\eta_\alpha$  of an NP embedded in a medium is given by [24]:

$$\sigma_\alpha = \frac{8\pi^2}{\lambda} R_p^3 \left[ \frac{\epsilon_p(\omega) - \epsilon_s}{\epsilon_p(\omega) + 2\epsilon_s} \right], \tag{9}$$

$$\eta_\alpha = \frac{\sigma_\alpha}{\pi R_p^2}. \tag{10}$$

The amount of laser energy required to be absorbed by unit volume of solution to produce heating effect is:

$$W = \frac{\sigma_\alpha}{\rho_p c_p} \int_0^t I dt, \tag{11}$$

where  $\rho_p$  and  $c_p$  are density and specific heat capacity of GNU, respectively, and the heat power generated by GNU ensemble is:

$$P = \sigma_\alpha I, \tag{12}$$

where  $I$  ( $\text{W cm}^{-2}$ ) is the intensity of laser light:

$$I = 1/2 c \epsilon_w |E_0|^2 \tag{13}$$

and

$$E = E_0 \frac{3\epsilon_s}{\epsilon_p + 2\epsilon_s}. \tag{14}$$

Using the above values in Eqs. (9) and (10) yields  $\sigma_\alpha \approx 1.35 \times 10^{-15} \text{ m}^2$  and  $\eta_\alpha \approx 17 \times 10^{-2}$ . Taking the experimental values of laser power  $P \approx 25 \text{ mW}$ , spot area  $A \approx 1.25 \times 10^{-3} \text{ cm}^2$ , the amount of heat power generated by one GNU is  $P_1 = I \sigma_\alpha \approx 2.7 \times 10^{-14} \text{ W}$ . Assuming that the pump beam irradiating the sample is cylindrical and the volume element,  $V_{e1} \approx \pi r_p^2 L \approx 1.25 \times 10^{-3} \text{ cm}^3$  consists of  $6.3 \times 10^6$  GNU given that a total of  $3.84 \times 10^9 \text{ NP/mL}$  is provided by the supplier. Therefore, the total power and heat generated per unit of volume element are  $P_T \approx 1.7 \times 10^{-7} \text{ W}$  and  $Q_T \approx 1.4 \times 10^{-3} \text{ W cm}^{-3}$ , respectively, which is detected by the probe beam. However, in an aqueous medium-containing NPs, clusters can act as the amplification factor and one can express the normalized  $\eta_\alpha$  for the NP geometrical cross section [22]:

$$\eta_\alpha = \frac{\sigma_\alpha}{G(t)\pi R_p^2}. \tag{15}$$

The clusters can result in enhanced thermal effects, since heat flow from individual NPs can be added [42]:

$$Q(r, t) = \sum_n q_n(t) \delta(r - r_n), \tag{16}$$

where  $q_n(t)$  represents the heat produced by  $n$ -GNU and  $r$  is the coordinate position, i.e., the distance from the center of GNU and the heat generated by the ensemble per unit time is:

$$Q(r, t) = -\frac{1}{2} \text{Re} \left[ i\omega \frac{\epsilon_p(\omega) - 1}{4\pi} \right] \sum_n \int \tilde{E}(r) \tilde{E}^*(r) d^3r. \tag{17}$$

Since the optical interaction and the photothermal effects under the plasmon resonance conditions are strongly dependent on the size and shape of the nanoparticle, therefore, the geometrical factor,  $F_g$  of NP shape should be considered [30]:

$$F_g = \sum_i \sum_j (A^{-1})_{ij}, \tag{18}$$

where the matrix  $A_{ij}$  is

$$A_{ij} = \frac{1}{|r_i - r_j|}, \tag{19}$$

and the position vectors  $r_i$  and  $r_j$  of the points are inside the NP. In the case of non-spherical NPs such as GNU, the main contribution to the effective radius comes from the furthest points, i.e., the tips of the star. In practice,  $N$  number of GNU with  $n$  tips can be agglomerated in a 3D random lattice cluster with different spherical harmonics orientation where the distance of the surface from the origin indicates the value of scalar spherical harmonics  $Y_l^m(\theta, \phi)$  in angular direction  $(\theta, \phi)$ . Here,  $l$  and  $m$  represent the degree and order of harmonic, and  $\theta$  and  $\phi$  show the angle between radius vector and  $+z$  axis and the angle between the projection of the radius vector in  $XY$  plane and  $+x$  axis, respectively. It has been suggested [30, 58] that GNU are potentially suitable heat source and superior to spherical NPs due to a more efficient heating effect because of their temperature relative factor,  $F_T$  being larger than 1 and higher the number of tips, the greater the  $F_T$ . Recently, we suggested that the temperature rise due to the gold nanoshells ensemble within the water can be governed by their arrangement, density, and potential for aggregation [59]. Therefore, the clustering results in a stronger surface plasmon absorption of light and more efficient photothermal effects, which are excellent candidates for hyperthermia tumour therapy [60]. Indeed, the effects of local accumulation or clustering under optical

interaction irradiation are different from dispersed conditions within the medium. Also, it has been demonstrated that at higher GNP concentrations, the probe deflection increases due to a steeper thermoelastic gradient as a result of higher absorption by particle agglomerates and particle size-dependent dispersions [32]. The time- and space-dependent temperature distribution around optically stimulated PNP is described by the differential equation for thermal diffusion [61]:

$$\rho_p(r) c_p(r) \frac{\partial T(r, t)}{\partial t} = K_w \nabla^2 T(r, t) + \langle Q_s(r, t) \rangle, \quad (20)$$

where  $T$  is the local temperature,  $K$  is thermal conductivity, and  $Q$  is the heat source generated by the GNU ensemble. After a transient evolution of temperature, materials reach steady-state temperature profile under CW illumination:

$$\tau_s = \frac{\rho_s c_s R_p^2}{K_s} = \frac{R_p^2}{D_s}, \quad (21)$$

$$\tau_p = \frac{\rho_p c_p R_p^2}{K_p} = \frac{R_p^2}{D_p}, \quad (22)$$

where  $D_t = K/\rho c$  is thermal diffusivity ( $\text{m}^2 \text{s}^{-1}$ ), and  $\tau_s$  and  $\tau_p$  represent the characteristic times associated with the evolution of the temperature profile in the surrounding PS and inside GNU, respectively. Given  $D_t^s \approx 1.3 \times 10^{-7} \text{ m}^2 \text{ s}^{-1}$  (i.e., PS and water are very similar) and  $D_t^p \approx 1.2 \times 10^{-4} \text{ m}^2 \text{ s}^{-1}$ , then  $\tau_s \approx 19 \text{ ns}$  and  $\tau_p \approx 20 \text{ ps}$ . Therefore, thermalization inside the nanoparticle happens much faster than the PS, as  $D_p$  is larger than  $D_s$ ; hence, the best consideration of reaching a comprehensive temperature profile of the total system is directed by the time scale  $\tau_s$  [62]. In the final steady-state regime, Eq. (20) reduces to:

$$K \nabla^2 T(r, t) = -\langle Q_s(r, t) \rangle. \quad (23)$$

This equation is formally equivalent to Poisson’s equation and produces a profile of temperature increase  $\Delta T$  given by a Coulomb potential outside the particle [24]:

$$\Delta T_p(r, t) = \frac{P}{4\pi K_s r} = \frac{\sigma_\alpha I}{4\pi K_s r} \quad r \geq R_p. \quad (24)$$

Substituting the Eqs. (9), (13), and (14) in Eq. (24) and simplifying give the temperature increase at the surface of GNU (i.e.,  $r = R_p$ ) [63]:

$$\Delta T_p(r, t) = \frac{IK_p R_p^2}{K_s} \text{Im} \left( \frac{\epsilon_p - \epsilon_s}{\epsilon_p + 2\epsilon_s} \right) \approx 2 \times \frac{IK_p R_p^2}{K_s}, \quad (25)$$

and the temperature per unit volume element is:

$$\Delta T_{\text{max}/e}(r, t) = NP_s / e \frac{R_p}{R_e} \Delta T_p. \quad (26)$$

Using the corresponding values  $K_p = 314 \text{ W m}^{-1} \text{ K}^{-1}$  and  $K_s = 0.6 \text{ W m}^{-1} \text{ K}^{-1}$  (i.e., PBS and water are very similar) in Eq. (25), it yields  $\Delta T_p(r, t) \approx 5 \times 10^{-11} \text{ K}$ , and substituting this in Eq. (26), we obtain  $\Delta T_{\text{max}/e} \approx 8 \times 10^{-7} \text{ K}$ . Equation (25) shows that the temperature of the system containing plasmonic nanoparticles is proportional to the square of the nanoparticle radius, i.e.,  $\Delta T \propto R_p^2$ . The size dependence of the temperature increase is governed by the total rate of heat produced and by the heat transfer through the NP. In the case of a mixed solution, the value of thermal conductivity of the mixed colloid depends on factors such as volume fraction, NP size, morphology, additives, pH, temperature, base fluid, and NP material [64]. Using the first-order approximation of Maxwell’s equation for effective thermal conductivity of GNU colloid [65]:

$$K_{\text{eff}} = \frac{K_s V_s + K_p V_p}{V_s + V_p}. \quad (27)$$

Substituting, the values of  $K_p$  and  $K_s$  in Eq. (27) yield  $K_{\text{eff}} \approx 196$  and  $157 \text{ W m}^{-1} \text{ K}^{-1}$  for S2 and S3, respectively, which corresponds to  $\Delta T_p(r, t) \approx 1.96 \times 10^{-11}$  and  $1.57 \times 10^{-11}$ , respectively, so that  $\Delta T_p(S1) > (S2) > (S3)$  as expected. Also, the corresponding thermal diffusivity in fractional volumes are determined as  $4.5 \times 10^{-4}$  and  $2 \times 10^{-4} \text{ m}^2 \text{ s}^{-1}$  for S2 and S3, respectively. Therefore, following the local heating and temperature rise, spatial thermal distribution occurs in the colloidal medium, which is stronger for the higher volume fraction.

As it was mentioned, information regarding the heat distribution of nanoparticles in biological tissues is an important issue in laser therapeutic applications. The temperature of NPs increases with characteristic time that is proportional to the surface and inversely proportional to heat diffusivity of surrounding medium such as biological medium. In the case of uniform distribution of GNU, the probability distribution is given by sum of Dirac delta function, which reduces to the single particle distribution. If, however, the distribution is random and that the density of NPs is spatially modulated due to, for example, laser electric field intensity oscillation or Brownian motion in static situation as it may be assumed in localized tumor treatment, then the population density, i.e., the concentration, may decrease as it move away from the center of target, as shown in Fig. 9. A factor which can complicate the situation is the geometrical form of NPs as the total heating effect is a combined effect of all GNU in both states of individual dispersed and agglomerate as well as their modulated space density distribution. This is because the biological tissue response to  $N$  particles heating system has the form of a convolution product involving the

spatial density distribution function,  $\rho_N(q)$ , and single particle heating temperature,  $T_1$ . For a modulated space-dependent distribution, as in our case, the spatial density variation should be considered where the average temperature increase due to many particles is:

$$\langle \Delta T_N(r, t) \rangle = \int d^3 r' \Psi_N(r') \Delta T_1(r - r', t), \tag{28}$$

where  $\Psi_N(r') d^3 r'$  is the probability of finding a particle at position  $r'$  in a finite volume  $d^3 r'$ . Normally, in soft matter physics and Brownian motion of colloidal dispersion which resembles a soft tissue, Lorentzian distribution model can be considered [25]:

$$\rho_N(q) = \frac{NR_p}{r_b} \frac{1}{1 + q^2 r_b^2} \Delta T_1(q, t); \tag{29}$$

the term  $(1 + q^2 r_b^2)^{-1}$  represents a spatially modulated decrease of temperature and  $q$  is the Fourier variable conjugate of  $r$ .

### 3.2 Probe beam deflection

When a laser beam interacts with an absorbing medium such as gold colloidal solution, highly localized heating occurs which causes thermal expansion and consequently a decrease in medium density. This will result in a macroscopic spatial gradient in the refractive index of the medium due to a temperature gradient,  $\partial n / \partial T$ , which is proportional to the beam intensity profile in the solution and hence redistribute the concentration of GNU. For most materials, the refractive index is smaller on the axis where absorption heating is highest. Therefore, the medium acts as a negative lens producing a mirage effect, and as the pump beam propagates through the medium, it gradually diverges and the probe beam deflects. The degree of both divergence and deflection depends on the pump laser power and the absorption coefficient of the sample. Depending on the sign of  $\partial n / \partial T$ , the index of refraction will be minimum for  $\partial n / \partial T < 0$  or maximum for  $\partial n / \partial T > 0$ . The radial changes the refractive index of the solution is:

$$\frac{\partial [\Delta T(r, z)]}{\partial r} = \frac{\gamma r_b^2}{4K_p} \frac{1}{r} \left( e^{-2r^2/r_b^2} - 1 \right) e^{-\alpha z}, \tag{30}$$

where  $\gamma = \alpha P / \pi r_b^2$  and  $P$  is the laser power. Therefore, thermal and concentration diffusion of GNU occur due to local heating by the laser beam inside the medium. The change of refractive index caused by SPR thermal heating as  $\Delta T(r) \propto R_p^2$  and concentration redistribution is given by:

$$\frac{dn(r, z)}{dT} = \left( \frac{\partial n}{\partial T} \right)_c + \frac{\partial n}{\partial c} \frac{\partial c}{\partial T}, \tag{31}$$

and the beam divergence angle,  $\theta_d$ , i.e., the angle between centered axis of the laser and the diverged beam rays or sometimes known as signal enhancement factor is [66]:

$$\theta_d = 1 - (1 + 2I)^{1/2} = \frac{dn}{dT} P / \lambda K_{\text{eff}}, \tag{32}$$

and so,  $\theta_d \approx 6.4^\circ \approx 124$  mrad for the pump beam, the thermo-optic coefficient of the mixture is calculated as  $dn/dT \approx -7.86 \times 10^{-4}$  and  $-6.3 \times 10^{-4} \text{ K}^{-1}$  for S2 and S3, respectively, which as expected are much larger than the value reported for water  $-0.8 \times 10^{-4} \text{ K}^{-1}$  [35]. Clearly, this indicates the role of thermal enhancement by PNP such as GNU in the medium, and secondly, higher concentrations will generate higher thermo-optic coefficient. Consequently, a PBD with an angle,  $\phi$ , proportional to the spatially varying refractive index gradient  $\nabla \perp n$  occurs integrated over the path of the beam through the excited region:

$$\phi = \frac{1}{n_0} \int_{\text{path}} \nabla \perp n ds, \tag{33}$$

where  $n_0$  is the refractive index of the initial or undisturbed medium and  $\perp$  denotes projection on the normal plane of the beam. It is assumed that the beam divergence,  $\theta$ , is small compared with the temperature distribution, which may be justifiable, since, typically, it is in the order of  $10^{-3}$  rad over 1 cm and the that the total deviations are smaller than the focused spot diameter of  $2f\lambda / \pi\phi_b = 120 \mu\text{m}$ , where  $f \approx 150$  mm is focal length of the lens and  $\phi_b \approx 1$  mm is the laser aperture diameter. The deflection of the beam due to the change in the index of refraction is detected by the lateral detector which converts the deflection into an output voltage. The PBD signal is proportional to the derivative of GNU concentration and the differentiation of the concentration gradient profile as a function of distance ( $x$ ) gives [67]:

$$\left( \frac{\partial C}{\partial y} \right) = - \frac{C_0}{2\sqrt{\pi Dt}} e^{(-y^2/4Dt)}, \tag{34}$$

where  $C_0$  is the initial concentration and  $D$  is the diffusion coefficient and the shape of the deflected beam trajectory inside the base fluid is [68]:

$$Z(y) = A e^{(-y^2/4Dt)}, \tag{35}$$

where  $A$  is a constant. It is seen from Eq. (35) that as time elapses, the concentration gradient vanishes. In biomedical therapeutic applications where nanoparticles such as gold are used for laser hyperthermia, the thermal effect depends on several influential parameters including laser power density, optical, and opto-thermal properties of tissue such as rate of denaturation and nanoparticles such as absorption and scattering cross sections. Therefore, the laser-tissue

thermal damage can be analyzed in terms of temporal and spatial temperature dependence, which, in turn, are affected by NPs' distribution.

## 4 Conclusion

The results showed that the GNU concentration affects the optical transmission and that it behaves non-linearly with laser power. The probe beam could detect the enhanced heat generation and the deflection responses exhibited a stochastic behaviour, which varied with positions in both  $x$ - and  $y$ -directions. Higher concentration produced a greater thermo-optic coefficient,  $S_2 > S_3 > \text{water}$ . The beam view and wavefront profiles demonstrated a non-uniform intensity distribution of warmer and cooler regions during the scanning process. The aberrations of the wavefronts confirmed by the Zernike coefficients and found in the order of  $S_2(20) > S_1(10) > S_1(20)$  consistent with PV wavefront slope and spatial period aberration relation. It is noteworthy that the aberration non-linear behaviour is consistent in all samples. It is believed that the study and knowledge about the net effect of a stochastic modulated spatial intensity distribution with strong and weak regions can help researchers in better understanding of laser–soft matter interaction and applications such as photothermal therapy of tumor treatment.

**Acknowledgements** Professor MEK greatly appreciates and acknowledges the support and research funding provided by MIS-Electronics R&D department.

## References

1. D. Lapotko, *Opt. Exp.* **17**, 2538–2556 (2009)
2. E. Ozbay, *Science* **311**, 189–193 (2006)
3. M. Gellner, B. Kustner, S. Schlucker, *Vib. Spect.* **50**, 43–47 (2009)
4. A. Haes, S. Zou, G. Schatz, *J. Phys. Chem. B* **108**, 109–116 (2004)
5. M. Tajabadi, M.E. Khosroshahi, Sh Bonakdar, *Opt. Photonics J.* **5**, 212–226 (2015)
6. H. He, Ch. Xie, J. Ren, *Anal. Chem.* **80**, 5951–5957 (2008)
7. M.E. Khosroshahi, M. Tajabadi, *J. Nanomed. Nanotechnol.* **8**, 1–10 (2017)
8. S. Park, J. Lee, T. Lee, S. Bae, *Int. J. Nanomed.* **10**, 261–270 (2015)
9. V.P. Pattani, J. Tunnell, *Lasers Surg. Med.* **44**, 675–684 (2012)
10. V.K. Pustovalov, L.G. Astafyeva, E. Galanzha, *Cancer Nano* **1**, 35–56 (2010)
11. M. Lechner, *J. Serb. Chem. Soc.* **70**, 361–369 (2005)
12. A.O. Pinchuk, G.C. Schatz, *Appl. Phys. B* **93**, 31–38 (2008)
13. C. Noguez, *J. Phys. Chem. C* **111**, 3806–3819 (2007)
14. H. Richardson, M. Carison, P. Tandler **9**, 1139–1146 (2009)
15. K. Yong, M.T. Swihart, H. Ding, *Plasmonics* **4**, 79–93 (2009)
16. M.E. Khosroshahi, A. Mandelis, B. Lashkari, *J. Biomed. Opt.* **20**, 1–12 (2015)
17. M.E. Khosroshahi, M. Asemani, *J. Mod. Phys.* **8**, 2219–2244 (2017)
18. H.Q. Xie, H. Lee, W. Youn, *J. Appl. Phys.* **94**, 4967–4974 (2003)
19. X.L. Chu, A. Nikolov, D. Wasan, *Langmuir* **12**, 5004–5010 (1996)
20. D. Lapotko, *Int. J. Heat Mass Tran.* **52**, 1540–1543 (2009)
21. Z. Liu, Y. Wu, Z. Guo, Y. Liu, *PLoS One* **9**, 1–11 (2014)
22. B. Khlebtsov, V. Zharov, A. Meluikov, V. Tuchin, *Nanotech.* **17**, 5167–5179 (2006)
23. M.E. Khosroshahi, L. Ghazanfari, P. Khoshkenar, *J. Mod. Phys.* **5**, 2125–2141 (2014)
24. G. Baffou, R. Quidant, *Laser Photonics Rev.* **7**, 171–187 (2013)
25. B. Fasla, A. Senoudi, A. Boussaid, *J. Biomat. Nanobiotech.* **2**, 49–54 (2011)
26. V. Giannini, R. Rodriguez-Olivros, A. Sanchez-Gil, *Plasmonics* **5**, 99–104 (2010)
27. S.D. Indrasekara, S. Meyers, S. Shubeita, L.C. Feldman, T. Gustafsson, L. Fabris, **6**, 8891–8899 (2014)
28. Z. Qin, Y. Wang, J. Randrianalisoa, V. Raeesi, *Sci. Rep.* **6**, 1–11 (2016)
29. H. Ma, P. Tian, J. Pello, L. Oddershed, *NanoLett.* **14**, 612–619 (2014)
30. R. Rodriguez-Oliveros, J. Sanchez-Gill, *Opt. Exp.* **20**, 621–626 (2012)
31. M.E. Khosroshahi, A. Mandelis, B. Lashkari, *J. Biomed. Opt.* **20**(1–2), 076009 (2015)
32. M.E. Khosroshahi, A. Mandelis, *Int. J. Thermophys.* **36**, 880–891 (2015)
33. J. Zhu, J. Shen, C. Hu, *Opt. Lett.* **27**, 1755–1757 (2002)
34. R. Silvia, M. de Araujo, P. Jail, S. Moreira, *AIP Adv.* **1**, 1–6 (2011)
35. R.D. Snook, R. Lowe, *Analyst* **120**, 2051–2054 (1995)
36. R. Elias, Q. Hassan, H. Sultan, A. Al-Asad, *Opt. Laser Tech.* **107**, 131–141 (2018)
37. A. Dhina, P. Palanisamy, *J. Biomed. Sci. Eng.* **3**, 285–290 (2010)
38. A. Tam, *Rev. Mod. Phys.* **58**, 381–431 (1986)
39. X. Yu, Y. Yao, Y. Sun, J. Tian, *Optik* **122**, 1701–1706 (2011)
40. I. Kwee, J.J. Braat, *Pure Appl. Opt.* **2**, 21–32 (1993)
41. D. Rativa, R. de Araujo, A. Gomes, B. Vohnsen, *Opt. Exp.* **17**, 2207–22047–22053 (2009)
42. J. Diaz, J. Fernandez-Dorado, C. Pizarro, J. Arasa, *J. Mod. Opt.* **56**, 149–155 (2009)
43. T. Salmon, C. van de Pol, *J. Cat. Ref.* **32**, 2064–2071 (2006)
44. M.S. Kirilenko, P. Khorin, A. Porfirev, *Comput. Opt. Nanophot.* **1638**, 66–75 (2016)
45. S. Brojabasi, V. Mahendran, B. Lahiri, J. Philip, *Opt. Comput. Sci.* **342**, 224–229 (2015)
46. B. Derjaguin, L. Landau, *Acta Physicochim. URSS* **14**, 633–662 (1941)
47. E. Verwey, J. Overbeek, *Theory of Stability of Lyophobic Colloids* (Elsevier Press, Amsterdam, 1948)
48. H. Loria, P. Pereira-Almao, C. Scott, *Ind. Eng. Chem. Res.* **50**, 8529 (2011)
49. S. Ganguly, S. Chakraborty, *Phys. Lett. A* **375**, 2394–2399 (2011)
50. A.O. Govorov, W. Zhang, T. Skeini, H. Richardson, *Nanoscale Res. Lett.* **1**, 84–90 (2006)
51. A. Polo, V. Kutchoukov, F. Bociort, S. Pereira, H. Urbach, *Opt. Exp.* **20**, 7822–7832 (2012)
52. J. Park, W. Lu, *J. Phys. Rev. E* **83**, 031402 (2011)
53. V. Slabko, A. Tsiptan, A. Aleksandrovsky, E. Slyuareva, *Appl. Phys. B* **117**, 271–278 (2014)
54. C. Bayer, S. Yun Nam, Y. Chen, *J. Biomed. Opt.* **18**, 016001 (2013)
55. J. Fan, L. Wang, *J. Heat Trans.* **133**, 04080-1-14 (2011)
56. Y. Yang, T. Ho, *Appl. Spect.* **41**, 583–585 (1987)
57. P. Jain, *J. Phys. Chem. B* **110**, 7238–7248 (2006)
58. S.V. Perminov, V.P. Drachev, S. Rautian, *Opt. Exp.* **15**, 8639–8648 (2007)



59. L. Ghazanfari, M.E. Khosroshahi, *Mat. Sci. Eng. C* **42**, 185–191 (2014)
60. M.E. Khosroshahi, L. Ghazanfari, Z. Hassannejad, S. Lenhart **4**, 1–9 (2015)
61. M. Ortega, L. Rodriguez, J. Piscitelli, A. Fernandez, *J. Opt. A Pure Appl. Opt.* **10**, 1–4 (2008)
62. G. Baffou, H. Rigneault, *Phys. Rev. B* **84**, 035415 (2011)
63. A. Govorov, H. Richardson, *Nano Today* **2**, 30–38 (2007)
64. P. Shima, J. Philip, *Indust. Eng. Chem. Res.* **53**, 980–988 (2013)
65. Y. Xuan, Q. Li, *Heat Fluid Flow* **21**, 58–64 (2000)
66. F. Cuppo, A. Figueirds Neto, S. Gomez, *J. Opt. Soc. Am. B* **19**, 1342–1349 (2002)
67. W. Jost, *Diffusion of Solids, Liquids, Gases, Chapter I and XI*, III edn. (Academic Press, New York, 1952)
68. A. Kurian, C. Bindhu, S. Harilal, R. Issac, *PRAMAN J. Phys.* **43**, 401–406 (1994)

**Publisher's Note** Springer Nature remains neutral with regard to jurisdictional claims in published maps and institutional affiliations.